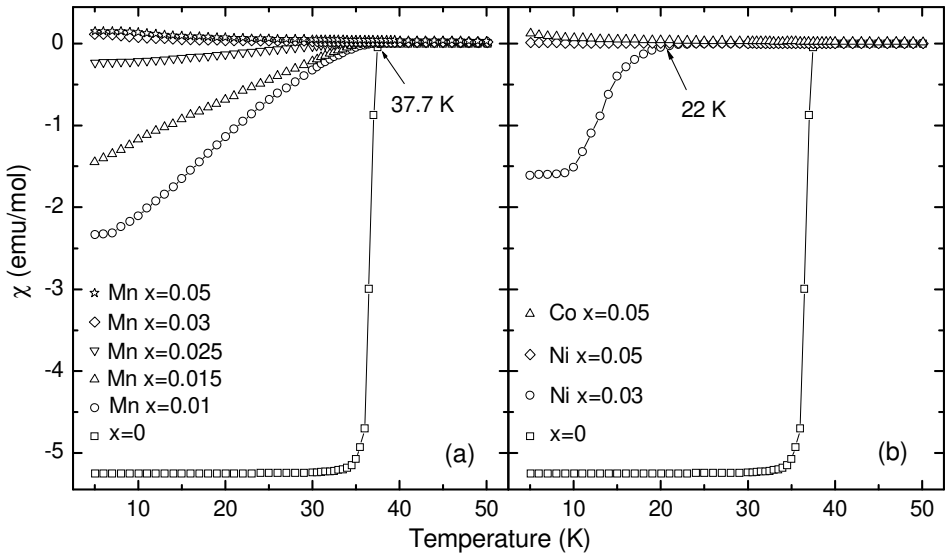

Fig. 1. Temperature dependence of magnetic susceptibility for $La_{1.85}Sr_{0.15}Cu_{1-x}M_xO_4$ (M=Mn, Ni, Co) single crystal samples. The applied magnetic field is 10 Oe with field-cooling. The magnetic field is applied perpendicular to the CuO_2 plane.

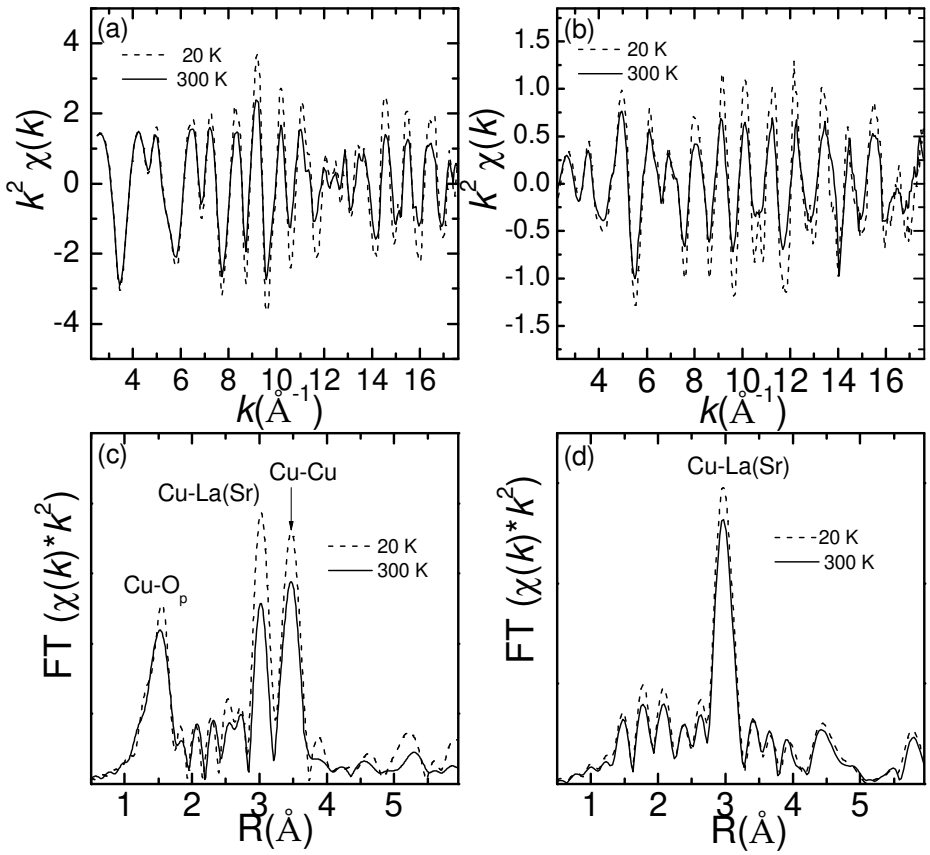

Fig. 2. (a) In-plane polarized Cu *K*-edge EXAFS oscillations (weighted by k^2) for $La_{1.85}Sr_{0.15}CuO_4$ at 20 K and 300 K. (b) Out-of-plane polarized Cu *K*-edge EXAFS oscillations (weighted by k^2) for $La_{1.85}Sr_{0.15}CuO_4$. (c) Magnitude of the complex FT of $k^2\times\chi(k)$ for $La_{1.85}Sr_{0.15}CuO_4$ in the CuO_2 plane at 20 K and 300 K. (d) Magnitude of the complex FT along the *c*-axis.

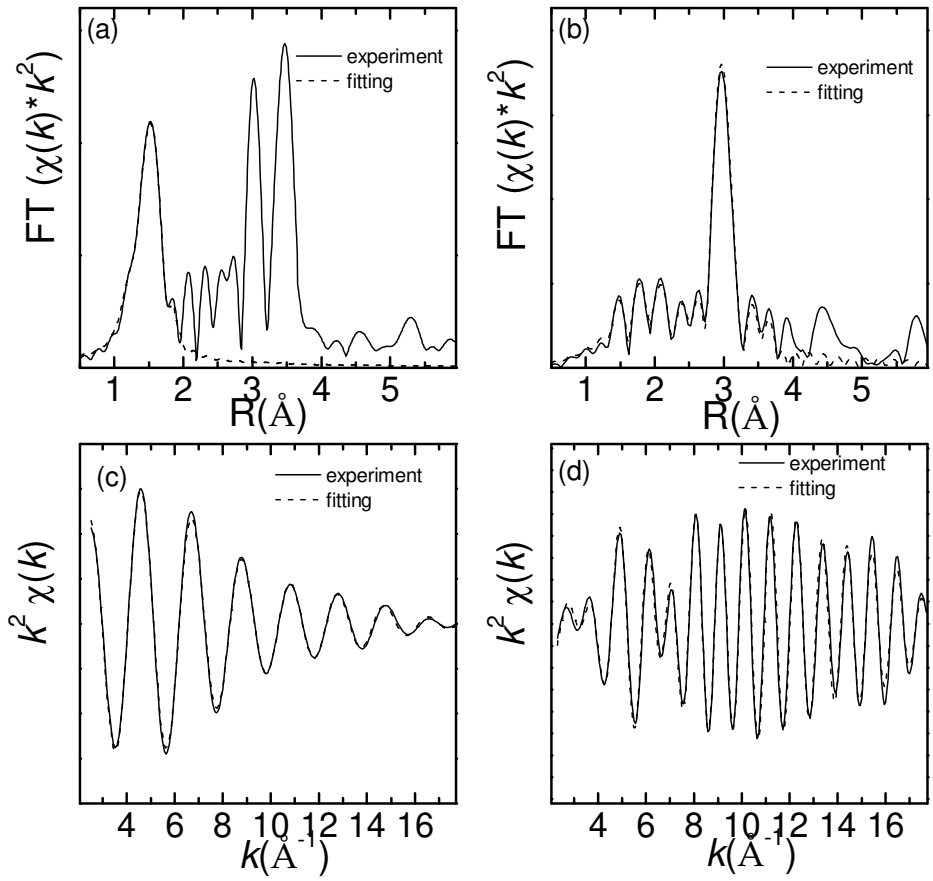

Fig. 3. (a) Comparison of the fitted curve on the nearest-neighbor Cu-O bond (dashed curve) with the experimental FT magnitude function within the CuO_2 plane at 300 K (solid curve). (b) Comparison of the fitted curve with the experimental FT magnitude function along the *c*-axis at 300 K. (c) The back-transformed EXAFS oscillation for the in-plane Cu-O bond at 300 K (solid curve, back-transformed over 0.9<R<2.0 Å). The dashed curve is the fitting result on the Cu-O bond. (d) The back-transformed out-of-plane EXAFS oscillation at 300 K (solid curve, back-transformed over 1.2<R<3.8 Å). The dashed curve is the fitted curve.

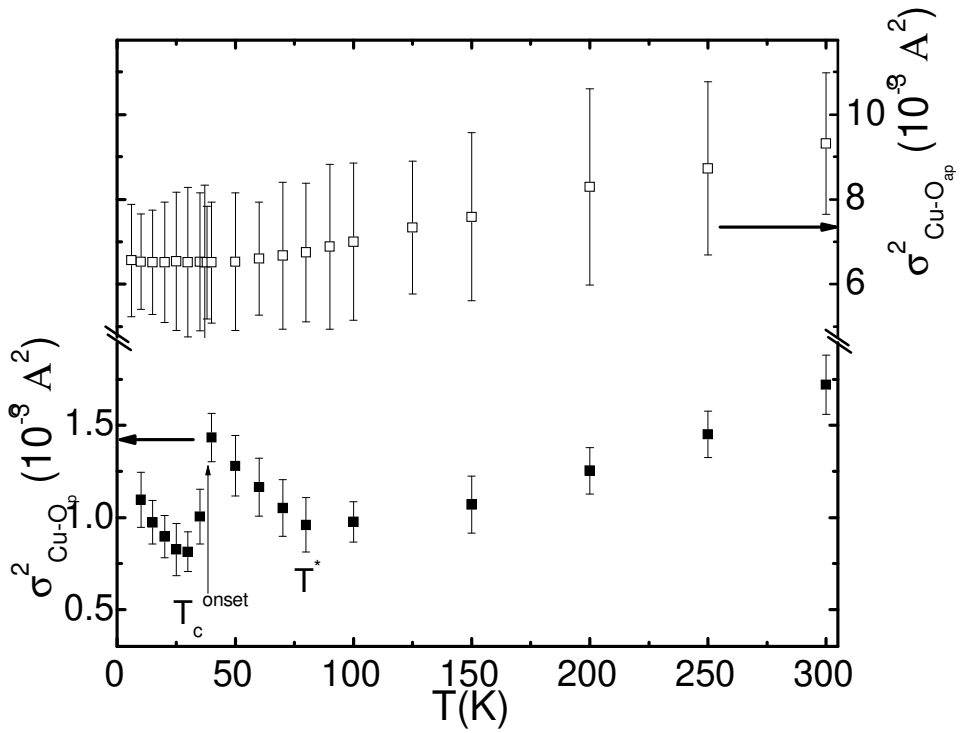

Fig. 4. Temperature dependence of $\sigma^2_{Cu\text{-}Op}$ and $\sigma^2_{Cu\text{-}Oap}$ for $La_{1.85}Sr_{0.15}CuO_4$. The error bars are estimated from the square root of the diagonal elements of the correlation matrix.

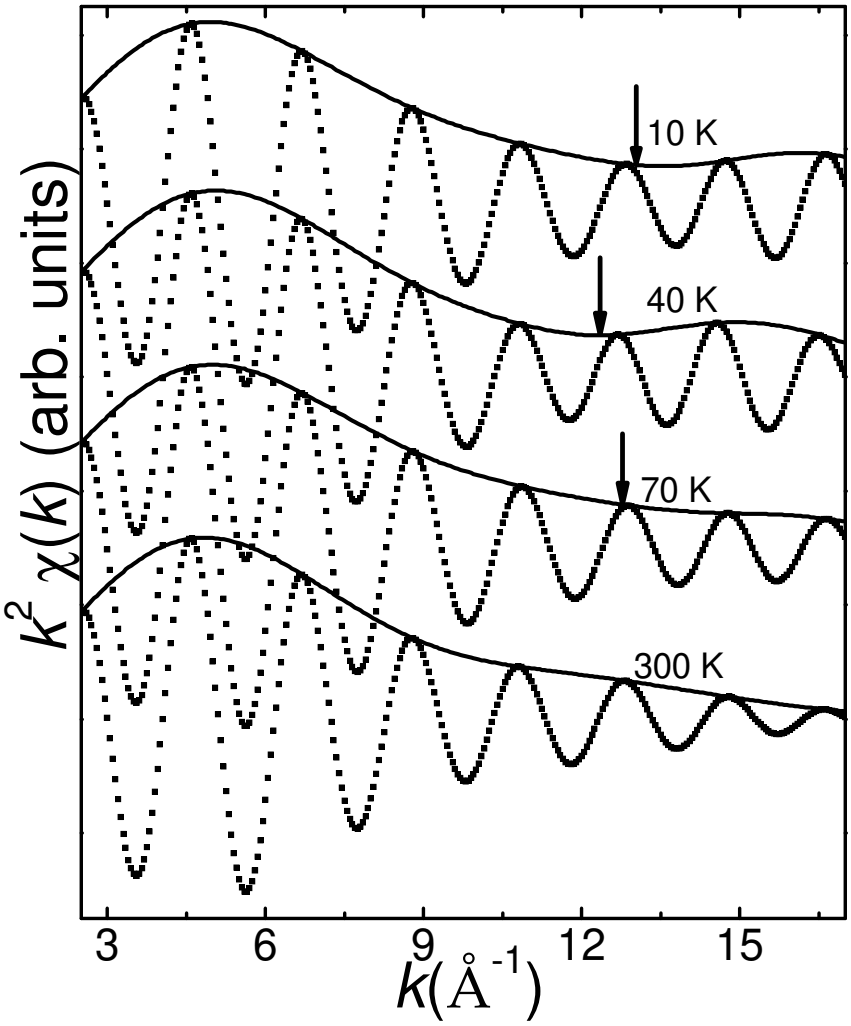

Fig. 5. Fourier-filtered (back-transformed over 0.9<R<2.0 Å) EXAFS oscillations (scattered dots) and amplitudes (lines) of the in-plane Cu-O_p bond. The changes with temperature in the FT moduli are reflected in the beat at about k≈12.5 Å.

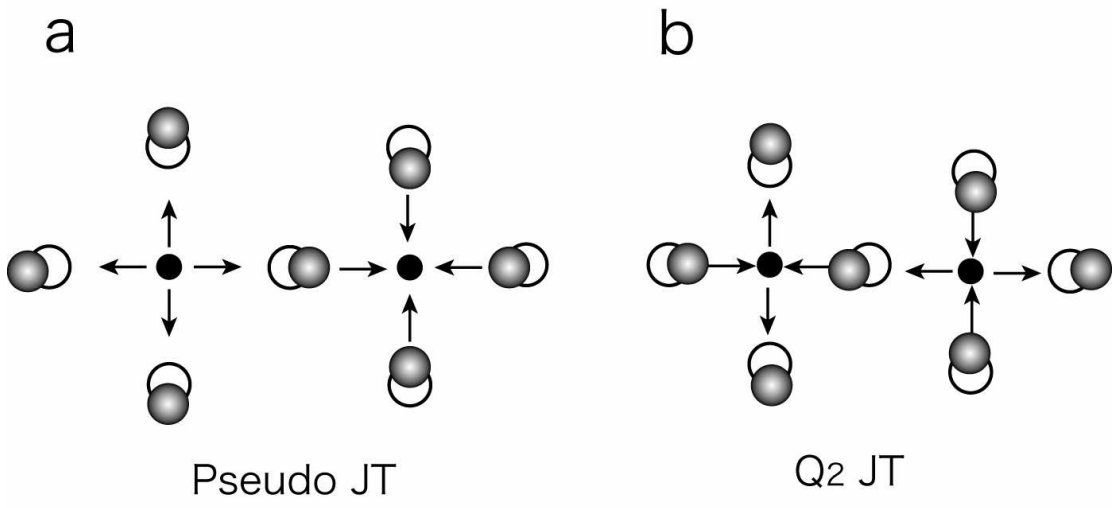

Fig. 6. Schematic pictures of the possible lattice modes describing the oxygen displacements: (a) pseudo-Jahn-Teller mode; (b) Q_2-type Jahn-Teller mode.

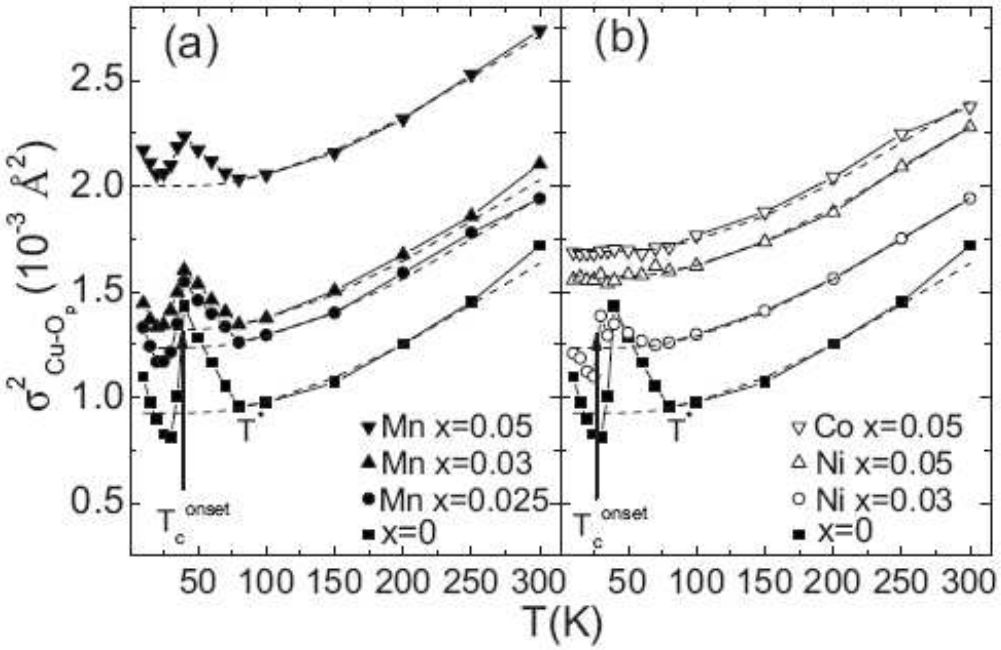

Fig. 7. Temperature dependence of the in-plane Cu-O bond MSRD σ^2_{Cu-Op} for $La_{1.85}Sr_{0.15}Cu_{1-x}M_xO_4$ (M=Mn, Ni, Co) samples. The dashed lines are the values calculated using equations (1) and (2).

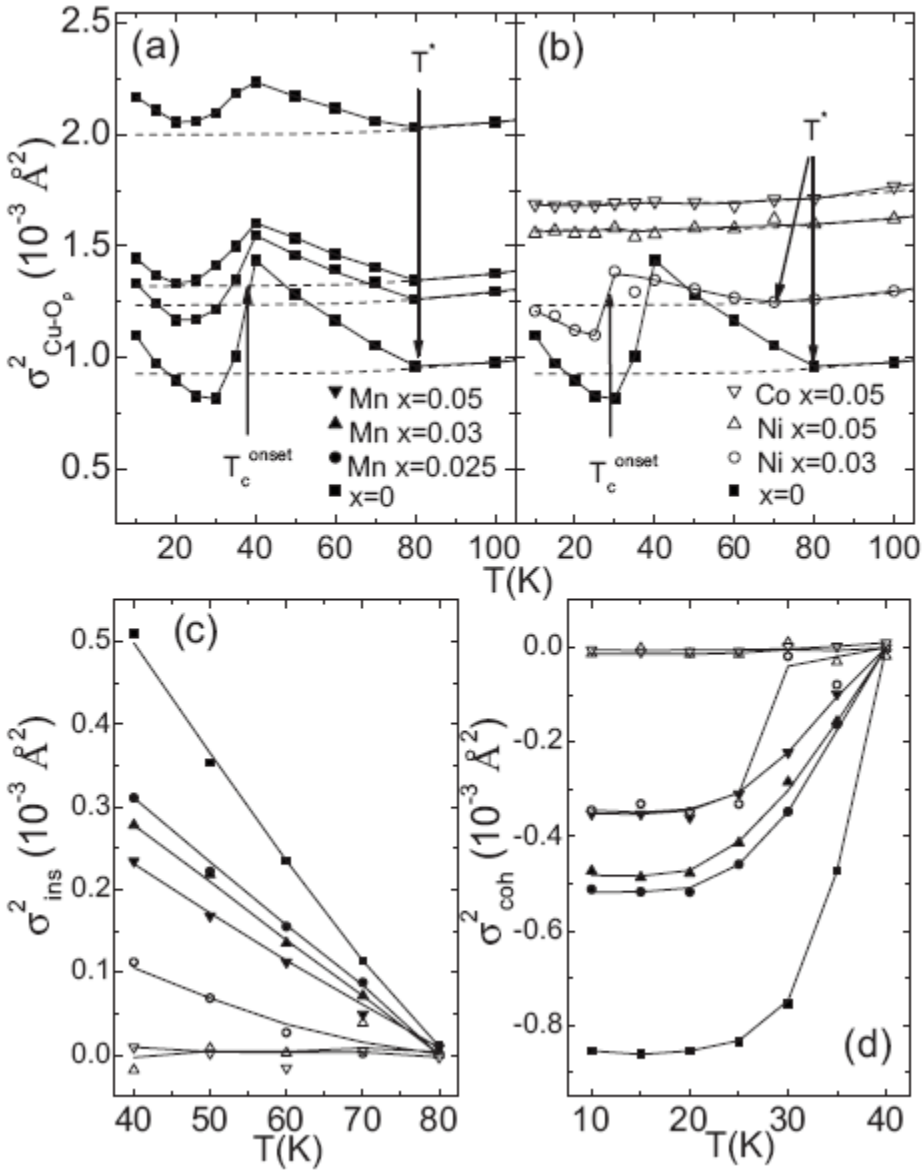

Fig. 8. (a) and (b) Expanded view of the MSRD of the in-plane Cu-O bond, σ^2_{Cu-Op} for $La_{1.85}Sr_{0.15}Cu_{1-x}M_xO_4$ (M=Mn, Ni, Co) samples below 100 K. (c) and (d) The magnitudes of the upturn at T^* (σ^2_{ins}) and the drop at T_c (σ^2_{coh}) as a function of temperature. The symbols in (c) and (d) are consistent with those in (a) and (b). The dashed lines in (a) and (b) are the calculated values using equations (1) and (2). The solid lines are guided to the eyes.

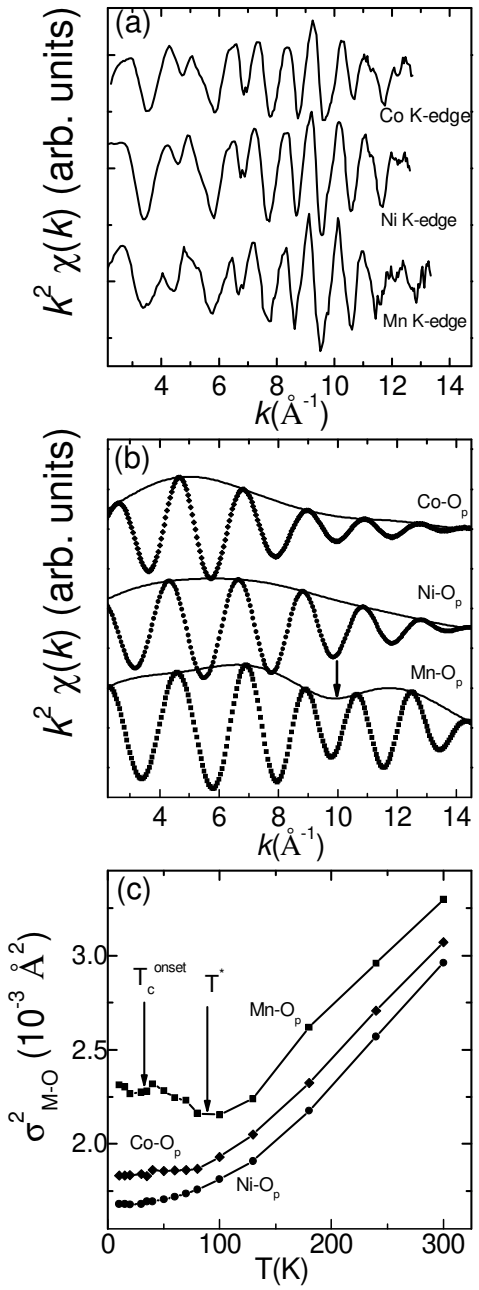

Fig. 9. (a) The in-plane Mn, Ni, and Co *K*-edges EXAFS oscillations (weighted by k^2) of $La_{1.85}Sr_{0.15}Cu_{1-x}M_xO_4$ (M=Mn, Ni, Co) with x=0.05 at 40 K. (b) Fourier-filtered EXAFS oscillations and amplitudes of the in-plane M-O bond at 40 K. (c) Temperature dependence of $\sigma^2_{M\text{-}Op}$ for the x=0.05 samples.

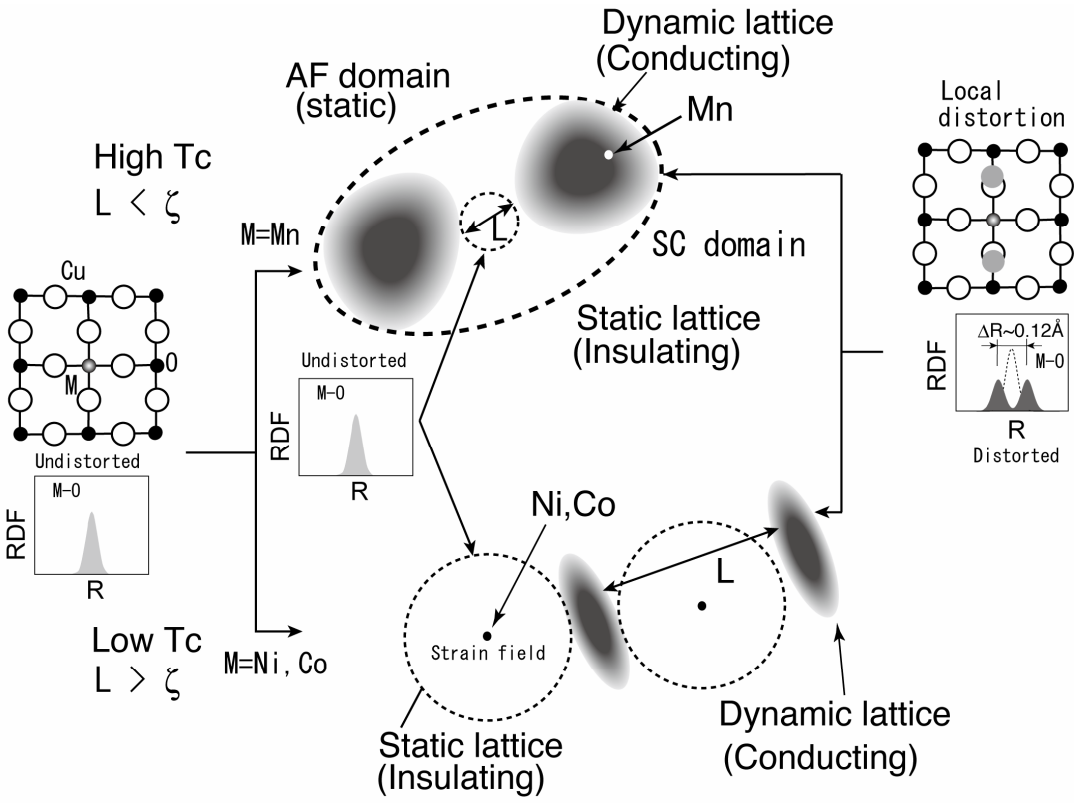

Fig. 10. Schematic of electronic inhomogeneity model illustrating the different perturbations on the local lattice structure induced by Mn, Ni, and Co doping. Dynamic metallic domains (shaded by grey color) are formed as the result of electronic phase separation. Mn dopants do not suppress the dynamic lattice instability. Ni and Co dopants disrupt the dynamic local lattice fluctuation around them and lead to the formation of static distorted domains (circled area) due to the effect of strain field.